Nano Research
2020, 13(5): 1389–1398
ISSN 1998-0124 CN 11-5974/O4
https://doi.org/10.1007/s12274-020-2646-7

Research Article

Multifunctional oxygen-enriching nano-theranostics for cancer-specific magnetic resonance imaging and enhanced photodynamic/photothermal therapy

Li Zhang[1,§], Zhe Yang[1,§], Jinghua Ren[4], Li Ba[4], Wenshan He[2] (✉), and Chun-Yuen Wong[1,3] (✉)

[1] *Department of Chemistry, City University of Hong Kong, Hong Kong, China*
[2] *Department of Breast and Thyroid Surgery, Union Hospital, Tongji Medical College, Huazhong University of Science and Technology, Wuhan 430022, China*
[3] *State Key Laboratory of Terahertz and Millimeter Waves, City University of Hong Kong, Hong Kong, China*
[4] *Cancer Center, Union Hospital, Tongji Medical College, Huazhong University of Science and Technology, Wuhan 430022, China*
[§] *Li Zhang and Zhe Yang contributed equally to this work.*

Received: 31 October 2019 / **Revised:** 31 December 2019 / **Accepted:** 7 January 2020

ABSTRACT

The combination of photodynamic therapy (PDT) and photothermal therapy (PTT) has attracted much interest in recent years, but non-specific distribution of photosensitizers and intrinsic tumor hypoxic microenvironment have continued to limit its therapeutic efficiency. We herein report a nano-theranostic system, denoted as Ce6-CuS/MSN@PDA@MnO_2-FA NPs, which combines PDT, PTT, magnetic resonance (MR) imaging with hypoxia-relieving and tumor-targeting functionalities. Central to this design is the use of mussel-inspired polydopamine (PDA) coating to encapsulate the chlorin e6 (Ce6) and copper sulfide nanoparticles (CuS NPs) loaded mesoporous silica nanoparticle (MSN) core. The PDA coating not only acts as pH sensitive gatekeeper to prevent the premature release of Ce6 under non-acidic tumor microenvironment (TME), but also facilitates post-functionalization so that hypoxia-relieving MnO_2 nano-sheets and tumor-targeting ligand folic acid-PEG-thiol (FA-PEG-SH) can be decorated on the outer part of the drug system. *In vitro* and *in vivo* measurements clearly demonstrated that all these functionalities worked synergistically as expected. The system, having a low dark cytotoxicity, can be effectively internalized by 4T1 cells and decrease the cell viability to 2% upon 660 nm/808 nm laser irradiation. Tumors in 4T1 tumor-bearing mice can almost be completely destroyed in 2 weeks via combined PDT/PTT. Together with the TME-sensitive MR imaging performance demonstrated, Ce6-CuS/MSN@PDA@MnO_2-FA NPs represent a multifunctional prototype which holds great potential to be developed into clinical theranostics.

KEYWORDS

hypoxia relief, MnO_2 nano-sheet, photodynamic therapy, photothermal therapy, magnetic resonance imaging

1 Introduction

Phototherapies such as photodynamic therapy (PDT) and photothermal therapy (PTT) have been widely recognized as promising alternatives to the traditional chemotherapy and radiotherapy used in cancer treatment [1, 2]. To achieve tumor destruction upon light irradiation, PDT employs photosensitizers that react with surrounding oxygen to generate reactive oxygen species (ROS) such as $^1O_2$, while PTT utilizes hyperthermia generated by photothermal agents [3–6]. Both PDT and PTT possess exceptional advantages of minimal invasiveness, low cumulative toxicity, reduced long-term mortality, and high therapeutic selectivity and efficacy [7, 8]. Unfortunately, the therapeutic performance of oxygen-dependent PDT is often severely limited within genuine tumor microenvironment (TME) where concentration of oxygen is usually low. Making the matter worse, the fast local-depletion of oxygen during PDT process further aggravates tumor hypoxia, resulting in low and unsustainable PDT efficiency [3, 9].

To date, several strategies have been explored to relieve tumor hypoxia for better PDT efficiency [10–13]. Considering the high level endogenous H_2O_2 (100 μM–1 mM) [14, 15] produced by the aberrant metabolism of cancer cells inside solid tumors, converting H_2O_2 into O_2 for PDT usage is an attractive strategy. Recently, catalytic decomposition of H_2O_2 by Prussian Blue nanoparticles (NPs) [16], platinum NPs [17] and nano-structured MnO_2 [14] has been demonstrated to improve the therapeutic efficacy of PDT. Among these catalysts, nano-structured MnO_2 possesses an attractive feature that the paramagnetic Mn^{2+} ions produced in the decomposition of MnO_2 in acidic medium allows T_1-magnetic resonance (MR) imaging for tumor detection [18]. Though nano-structured MnO_2 has received much attention and great progresses have been made in the development of various nano-theranostic reagents [18–21], there are shortcomings in these MnO_2-incorported nano-PDT systems, such as tedious synthesis procedures, poor physiological stability and organic solvents involvement. More importantly, these systems mainly rely on the enhanced permeability and retention effect as the drug delivery mechanism, meaning that they lack tumor selectivity

Address correspondence to Chun-Yuen Wong, acywong@cityu.edu.hk; Wenshan He, hewenshan@hust.edu.cn

and would induce undesirable side effects [22].

While introducing tumor-targeting functionality into the MnO_2-incorported nano-PDT systems can solve the tumor selectivity issue, it is well-known that single-modality therapy has limited therapeutic effect when compared with multi-modality therapy [23–25]. Therefore it is not uncommon to see PDT and PTT bundled onto one single nano-platform for combined therapy. Although multifunctional nano-drug delivery systems which allow combined PDT and PTT with hypoxia-relieving and tumor-targeting abilities are highly desirable, their development is significantly hampered by the complexity of synthesis and/or compatibility of different add-on functionalities [26, 27].

We herein report a rational design of nano-theranostic system, denoted as Ce6-CuS/MSN@PDA@MnO_2-FA NPs, which combines PDT, PTT, MR imaging with hypoxia-relieving and tumor-targeting functionalities. As shown in Scheme 1, the system has a thiol-functionalized mesoporous silica nanoparticle (MSN) core which is loaded with chlorin e6 (Ce6) and CuS as PDT and PTT agents, respectively. Central to this design is the use of polydopamine (PDA) to encapsulate the core for both gatekeeping and post-functionalization of the drug system. More specifically, the PDA coating (1) increases the dispersibility of the core, (2) acts as a smart pH sensitive gatekeeper to prevent the premature release of Ce6 under non-acidic TME, (3) reacts with $KMnO_4$ to give hypoxia-relieving MnO_2 nano-sheets, and (4) serves as a substrate for the conjugation with tumor targeting ligand folic acid PEG thiol (FA-PEG-SH) [28–30]. A noteworthy method, which is surfactant-free to generate CuS NPs *in situ* in the pores of MSN NPs, and a facile approach to prepare MnO_2 nano-sheets on PDA via the redox reaction between PDA and potassium permanganate ($KMnO_4$) under a mild condition, have been successfully developed. Moreover, it is encouraging that all the functionalities in our system work synergistically as designed. The NPs, having a low dark cytotoxicity (cell viability > 85% at 200 μg·mL^{-1}), can be effectively internalized by 4T1 cells. Upon 660 nm laser irradiation (50 mW·cm^{-2}, 10 min) (Ce6 concentration at 16 μg·mL^{-1} and CuS concentration at 60 μg·mL^{-1}) the cell viability decreases to 29%, whereas that of the Ce6-CuS/MSN@PDA-FA NPs (i.e. analogous system without MnO_2 nano-sheets) is 54%, signifying the hypoxia-relieving ability of the MnO_2 nano-sheets. The cell viability can be further decreased to 2% when both 660 and 808 nm lasers (50 mW·cm^{-2} and 2 W·cm^{-2} respectively, 10 min) are used for a combined PDT/PTT, and the tumors in 4T1 tumor-bearing mice can almost be completely destroyed in 2 weeks by the synergistic effects. Regarding the diagnostic ability, our system shows a TME-sensitive MR imaging performance with a calculated longitudinal relaxivity (r1) of 10.41 mM^{-1}·s^{-1}, which is 2 times higher than that of the clinical MR imaging agent Magnevist®.

2 Experimental

2.1 Materials

Tetraethoxysilane (TEOS, 98%), 3-mercaptopropyl trimethoxysilane (MPTMS, 95%), $KMnO_4$ (≥ 99%), copper chloride dihydrate ($CuCl_2·2H_2O$, ≥ 99.95%), sodium sulfide nonahydrate ($Na_2S·9H_2O$, ≥ 99.99%), hydrogen peroxide (H_2O_2, 30%), fetal bovine serum (FBS), Dulbecco's modified Eagle's medium (DMEM), Dulbecco's phosphate-buffered saline (DPBS), 2',7'-dichlorodihydrofluorescein diacetate (DCFH-DA, ≥ 97%) penicillin-streptomycin, trypsin, 3-(4,5-dimethylthiazol-2-yl)-2,5-diphenyltetrazolium bromide (MTT, 98%), 4',6-diamidino-2-phenylindole dihydrochloride (DAPI), propidium iodide (PI), and calcein acetoxymethyl ester (Calcein/AM) were purchased from Sigma-Aldrich. Hexadecyl trimethyl ammonium bromide (CTAB, 99%), sodium hydroxide (NaOH, 97%), dopamine hydrochloride (98%), and Ce6 (98%) were purchased from J&K Chemical Ltd. Hydrochloric acid (HCl, 36%–38%), nitric acid (HNO_3, 68%), methanol (≥ 99.7%), ethanol (≥ 99.7%) and dimethyl sulfoxide (DMSO, > 99.8%) were purchased from Sinopharm Chemical Reagent Co. Ltd. FA-PEG-SH (M_W =

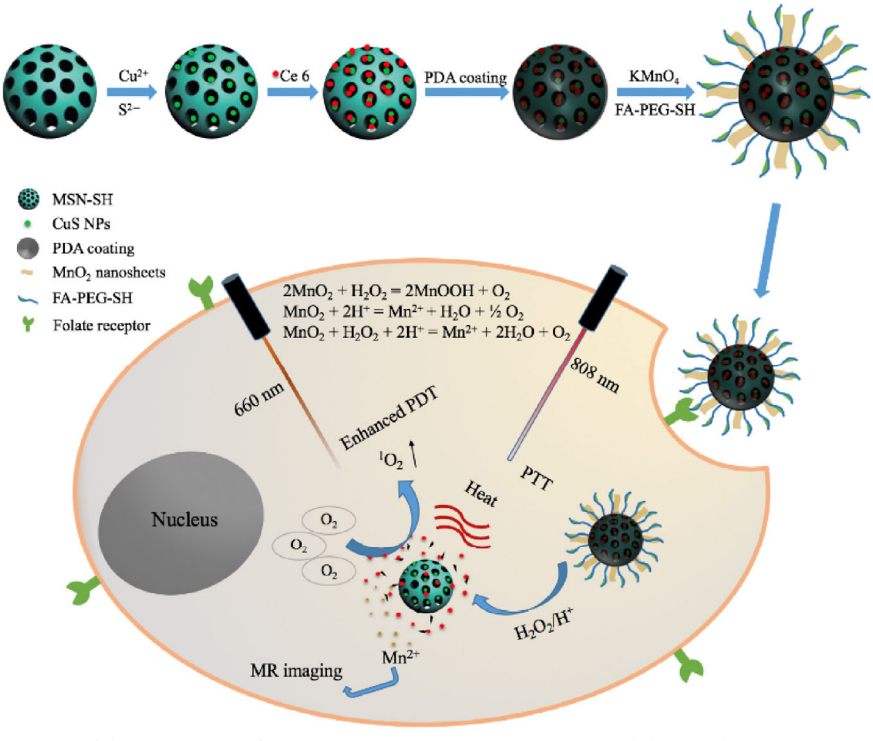

Scheme 1 Schematic illustration of the preparation of Ce6-CuS/MSN@PDA@MnO_2-FA NPs and their application in tumor-specific MR imaging and synergistically enhanced PDT/PTT.

2,000 Da, 95%) and 2,2,6,6-tetramethyl-4-piperidone (TMPD) were purchased from Aladdin Chemical Co. Ltd. All the reagents were used as received without any purification. Aqueous dilutions were prepared with deionized (DI) water.

2.2 Synthesis of Ce6-CuS/MSN@PDA@MnO_2-FA NPs

2.2.1 *Synthesis of CuS-loaded MSN NPs (CuS/MSN NPs)*

Thiol-functionalized MSN NPs (MSN-SH NPs) were synthesized according to a literature reported procedure [31]. 20 mg of MSN-SH NPs were dispersed in 20 mL of DI water (pH 7–8) and sonicated for 30 min. 200 μL of $CuCl_2{\cdot}2H_2O$ solution (1 M) was then added to the above mixture. After continuous stirring for 6 h, the resultant Cu^{2+}-loaded MSN NPs were collected by centrifugation. These NPs were re-dispersed in 20 mL of HCl-acidified DI water (pH 1) with sonication. A 400 μL of Na_2S solution (1 M) was then added and the mixture was allowed to react at 90 °C for 15 min. The resultant CuS/MSN NPs were collected by centrifuging the resultant green mixture and dried under vacuum (38.06 mg) for later use.

2.2.2 *Synthesis of Ce6-loaded CuS/MSN NPs with PDA coating (Ce6-CuS/MSN@PDA NPs)*

CuS/MSN NPs obtained in the previous step were first dispersed in 25 mL of methanol with sonication. 5 mL of Ce6 solution (1 mg·mL^{-1}) was then added, and the resultant mixture was gently shaken overnight in the dark at room temperature. The unloaded Ce6 was then removed by centrifugation, and the amount of encapsulated Ce6 was determined according to the absorbance changes at 665 nm. The drug loading content (DLC) and drug loading efficiency (DLE) were calculated according to the previous formulate [32]. For PDA coating, the Ce6-loaded CuS/MSN NPs (42.87 mg) were first dispersed in 25 mL of DI water (pH 8.5) and sonicated for 30 min. 4 mL of dopamine solution (5 mg·mL^{-1}, pH 8.5) was then added dropwise and the mixture was stirred for 6 h in the dark at room temperature. The resultant black Ce6-CuS/MSN@PDA NPs (50 mg) were collected by centrifugation and washed with DI water.

2.2.3 *Synthesis of MnO_2- and folic acid-functionalized Ce6-CuS/MSN@PDA NPs (Ce6-CuS/MSN@PDA@MnO_2-FA NPs)*

The above Ce6-CuS/MSN@PDA NPs dispersion (2 mL, 25 mg·mL^{-1}) was add to a 25 mL solution of $KMnO_4$ (0.2 mg·mL^{-1}) with vigorous stirring, and the mixture was allowed to react for 10 min. The resultant Ce6-CuS/MSN@PDA@MnO_2 NPs were collected by centrifugation, washed with DI water and then re-dispersed in DI water (25 mL, 2.1 mg·mL^{-1}, pH 9.0). Subsequently, 6 mL of FA-PEG-SH (5 mg·mL^{-1}, pH 9.0) solution was added dropwise into the Ce6-CuS/MSN@PDA@MnO_2 NPs dispersion and then kept for 48 h in the dark with gentle stirring. The resultant Ce6-CuS/MSN@PDA@MnO_2-FA NPs were collected by centrifugation, washed with DI water for several times, and then freeze dried (75.58 mg) for further use. The contents of CuS, Ce6, MnO_2, PDA and FA-PEG-SH in Ce6-CuS/MSN@PDA@MnO_2-FA NPs were determined to be 23.89%, 6.37%, 3.31%, 9.43% and 30.54%, respectively.

3 Results and discussion

3.1 Design, synthesis and characterization

The synthesis and working principle of our proposed Ce6-CuS/MSN@PDA@MnO_2-FA NPs is depicted in Scheme 1. PTT agent CuS was first immobilized onto thiol-functionalized MSN NPs with the use of $CuCl_2$ and Na_2S. This way, CuS can be generated *in situ* in the pore of MSN NPs without the use of any surfactant. The resultant CuS/MSN NPs were then loaded with PDT agent Ce6, followed by encapsulation with mussel inspired PDA coating for various purposes. Apart from improving the dispersibility of the Ce6-CuS/MSN core and preventing premature release of Ce6 under non-acidic TME, PDA can be functionalized with MnO_2 nano-sheet via a facile redox reaction between PDA and $KMnO_4$, and conjugated with folic acid-containing FA-PEG-SH to endow tumor targeting ability. Notably, all these synthetic steps are very straight-forward without compatibility issue. With this design, the endogenous H_2O_2 of the tumor can be efficiently converted to O_2 by the outer MnO_2 nano-sheets to relieve tumor hypoxia, leading to enhanced PDT efficiency. Combining with the excellent photothermal property of CuS NPs and PDA coating, Ce6-CuS/MSN@PDA@MnO_2-FA NPs are expected to deliver a synergetic PDT/PTT when simultaneously treated with 660 and 808 nm laser. Additionally, the paramagnetic Mn^{2+} produced from the degradation of MnO_2 nano-sheets under acidic pH can induce T_1-MR imaging for tumor diagnosis.

Transmission electron microscopy (TEM) was used to study the morphology, size, and dispersibility of CuS/MSN, Ce6-CuS/MSN@PDA NPs and Ce6-CuS/MSN@PDA@MnO_2-FA NPs. TEM image of the CuS/MSN NPs (Fig. 1(a)) shows an average particle size of 144 nm with excellent mono-dispersibility. Although the CuS NPs in the channels of MSN were hardly observed by high-resolution TEM (Fig. S1 in the Electronic Supplementary Material (ESM)) as reference mentioned [33, 34], TEM elemental mapping images of the CuS/MSN NPs suggest a thorough distribution of CuS in the MSNs (Fig. 1(d)). Compared with CuS/MSN NPs, Ce6-CuS/MSN@PDA NPs are slightly larger in size (160 nm) with obvious outer coating (Fig. 1(b)), indicating the presence of PDA. The deposition of MnO_2 nano-sheets further increases the size (182 nm) and surface roughness of the NPs (Fig. 1(c)). X-ray diffraction (XRD) analysis was also performed to get insight into the phase structures. As shown in Fig. S2 in the ESM, the characteristic diffraction peak around 21.2° found in all curves indicated the existence of MSN-SH; no significant changes were observed after loading Cu^{2+} on MSN-SH NPs. The diffraction peaks at 2θ = 27.74°, 29.31°, 31.82°, 32.92°, 48.16°, 52.68° and 59.36° for CuS/MSN NPs could be indexed to the (101), (102), (103), (006), (107), (108) and (116) planes of CuS NPs (JCPDS No. 79-2321). Additionally, the existence of PDA coating on Ce6-CuS/MSN@PDA@MnO_2-FA NPs was supported by the overlapped diffraction peak at 22.1°; the peaks at 2θ = 36.5° and 65.4° could be indexed to the (100) and (110) planes of δ-MnO_2 (JCPDS No. 18-0802). These results verified the successful generation of CuS NPs and MnO_2 nanosheets in the preparation of Ce6-CuS/MSN@PDA@MnO_2-FA NPs.

Dynamic light scattering (DLS) measurements were used to monitor the hydrodynamic size (D_h) of the NPs. The D_h of CuS/MSN NPs (145.3 nm) was similar to the result of TEM, indicating that the size and shape of CuS/MSN NPs were well maintained upon suspension in water. However, the D_h of Ce6-CuS/MSN@PDA and Ce6-CuS/MSN@PDA@MnO_2-FA NPs (170.5 and 203.7 nm, respectively) reveals that these NPs swell in water (Fig. 1(e)). The polydispersity indexes (PDI) of 0.158, 0.142 and 0.168 respectively suggest narrow particle size distribution in water. The zeta potential of Ce6-CuS/MSN@PDA@MnO_2-FA NPs was measured to be −26.52 ± 0.8 mV, which indicated the feasibility for biomedical applications. More importantly, the D_h (Fig. S3 in the ESM) and zeta potential (Fig. S4 in the ESM) of Ce6-CuS/MSN@PDA@MnO_2-FA

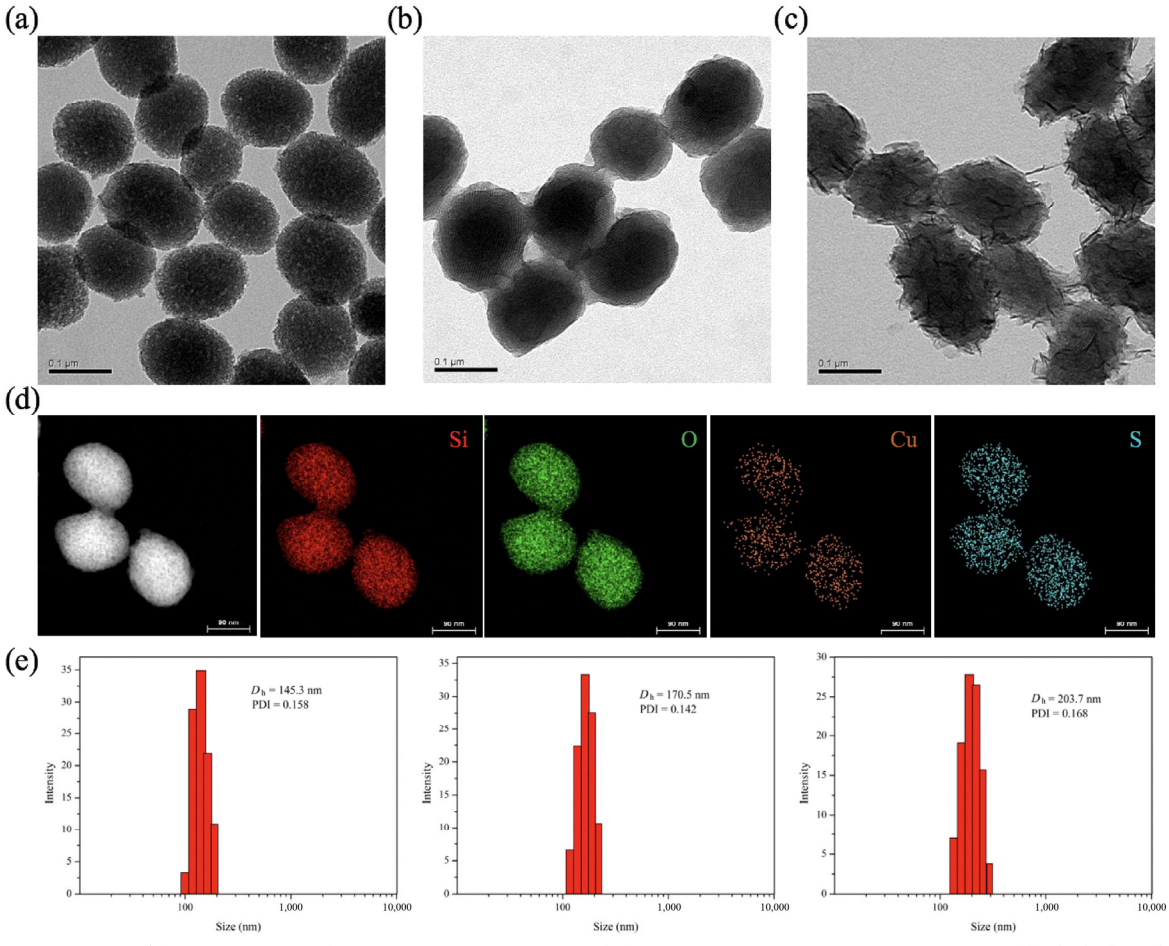

Figure 1 TEM images of (a) CuS/MSN NPs, (b) Ce6-CuS/MSN@PDA NPs and (c) Ce6-CuS/MSN@PDA@MnO_2-FA NPs NPs. (d) The high-angle annular dark-field (HAADF)-scanning TEM (STEM) image of CuS/MSN NPs, and corresponding TEM element mappings of the Si, O, Cu, S K-edge signals. (e) Hydrodynamic diameter and size distribution of CuS/MSN NPs, Ce6-CuS/MSN@PDA NPs and Ce6-CuS/MSN@PDA@MnO_2-FA NPs NPs, respectively.

NPs remain nearly the same before and after 7-day dialysis in PBS buffer and DMEM medium, revealing their excellent physiological stability.

The UV–vis–NIR absorption spectra for the NPs were depicted in Fig. 2(a). While bare MSNs are nearly optically transparent in the NIR region, CuS/MSN NPs show improved NIR absorption with peak maximum around 980 nm (observed at a higher concentration, see Fig. S5 in the ESM). Ce6-CuS/MSN@PDA NPs featured characteristic peaks at 405 and 665 nm, signifying the loading of Ce6; its improved NIR absorption is attributed to the presence of PDA coating. Finishing the NPs with MnO_2 nano-sheets and FA-PEG-SH gave an overlapping peak around 400 and an additional peak at 280 nm respectively. The colors for the NPs at different synthetic stages are shown in the inset of Fig. 2(a).

Ce6 was encapsulated into the pored structure of MSN with a pH sensitive PDA coating. The DLC and the DLE were calculated to be DLC = 11.0% and DLE = 96.3%, respectively. The drug release profiles of Ce6-CuS/MSN@PDA@MnO_2-FA NPs were clearly shown in Fig. 2(b). While the cumulative release of Ce6 was only 20.8% after 48 h at physiological pH (pH 7.4), this value increased to 52.1% at pH 5.0. These results demonstrated that PDA functioned as a pH sensitive gatekeeper to prevent the premature release of Ce6 under non-acidic TEM and facilitated drug release under acidic TEM [28, 30].

The photothermal property of Ce6-CuS/MSN@PDA@MnO_2-FA NPs originating from CuS and PDA was studied by irradiating the NPs using an 808 nm laser (2 W·cm^{-2}). As shown in Fig. 2(c), a concentration-dependent increase in temperature was clearly observed. Notably, an increase of 27.3 °C (from 23.5 to 50.8 °C) was recorded in the NPs dispersion of 200 μg·mL^{-1} after exposure to laser for 10 min (Fig. 2(d)). This is in contrast to the control group (pure water) that only a 2 °C increase was resulted under identical experimental conditions.

The ability for Ce6-CuS/MSN@PDA@MnO_2-FA NPs to catalyze the decomposition of H_2O_2 to generate O_2 was investigated by an oxygen probe [35]. As shown in Fig. S6 in the ESM and Fig. 3(a), obvious O_2 bubbles were produced from the H_2O_2 solutions in the presence of Ce6-CuS/MSN@PDA@MnO_2-FA NPs, and the size and amount of bubbles increased with the concentration of the NPs. Moreover, increased acidity of the solution led to accelerated O_2 generation (Fig. 3(b)), consistent with the chemical equations depicted in Scheme 1. These results indicated that our MnO_2-functionalized NPs possessed hypoxia-relieving ability by generating O_2 using H_2O_2 as feedstock.

3.2 Cellular uptake and cytotoxicity

To evaluate the feasibility of Ce6-CuS/MSN@PDA@MnO_2-FA NPs for biomedical applications, *in vitro* cellular uptake and cytotoxicity experiments were performed. Because of the fluorescent nature of Ce6, fluorescence imaging could be used to study the internalization of the Ce6-containing NPs by cells. As shown in Fig. 4(a), the localization of red fluorescence signals in 4T1 cells upon incubation with Ce6-CuS/MSN@PDA@MnO_2 and Ce6-CuS/MSN@PDA@MnO_2-FA NPs confirmed the cellular uptake of these NPs. Moreover, it was evidenced that conjugation of FA enhanced the cellular uptake

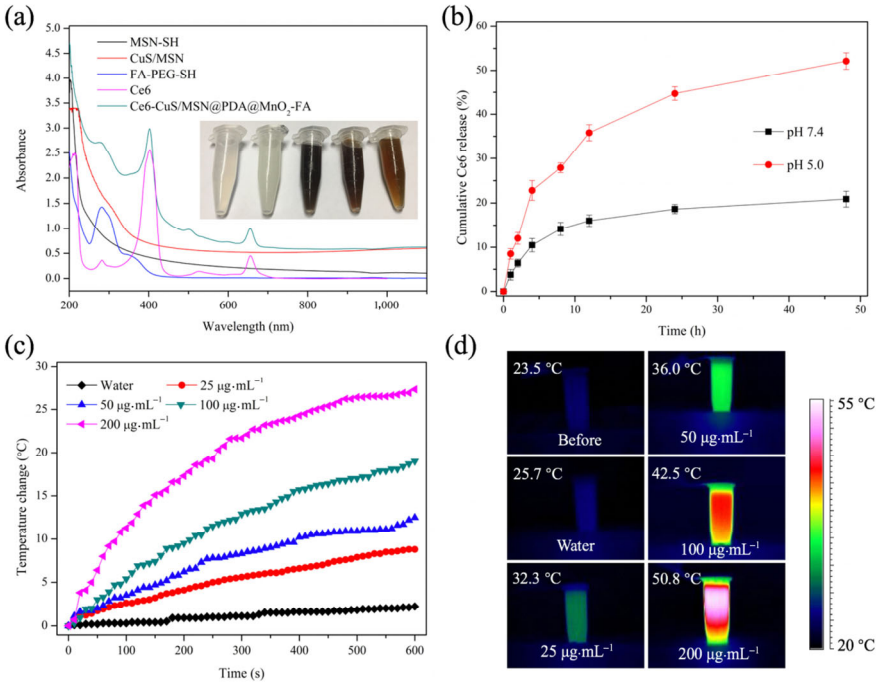

Figure 2 (a) UV–vis–NIR absorbance spectra of MSN-SH NPs, CuS/MSN NPs, Ce6-CuS/MSN@PDA@MnO_2-FA NPs, FA-PEG-SH and Ce6 in DI water. Inset shows the digital photos of the nanoparticles in DI water (MSN-SH, CuS/MSN, Ce6-CuS/MSN@PDA, Ce6-CuS/MSN@PDA@MnO_2 and Ce6-CuS/MSN@PDA@MnO_2-FA from left to right). (b) Cumulative Ce6 release profile of Ce6-CuS/MSN@PDA@MnO_2-FA NPs in PBS buffer with pH 7.4 and pH 5.0. (c) Temperature increase of Ce6-CuS/MSN@PDA@MnO_2-FA NPs aqueous dispersion with different concentrations under 808 nm laser irradiation (2 W·cm^{-2}) for 10 min. (d) Infrared thermographic images of before and after 10 min laser irradiation with different concentrations of Ce6-CuS/MSN@PDA@MnO_2-FA NPs aqueous dispersion.

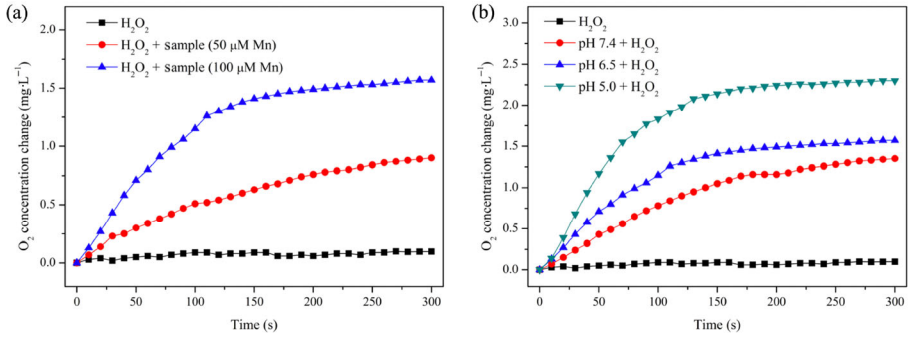

Figure 3 (a) O_2 generation by addition of H_2O_2 to Ce6-CuS/MSN@PDA@MnO_2-FA NPs aqueous dispersion (pH 6.5) with different concentrations ([Mn] 0, 50 or 100 μM). (b) O_2 generation by addition of H_2O_2 to Ce6-CuS/MSN@PDA@MnO_2-FA NPs aqueous dispersion ([Mn] 100 μM) under different pH values (pH 7.4, 6.5 and 5.0). Sample = Ce6-CuS/MSN@PDA@MnO_2-FA NPs, [H_2O_2] = 100 μM.

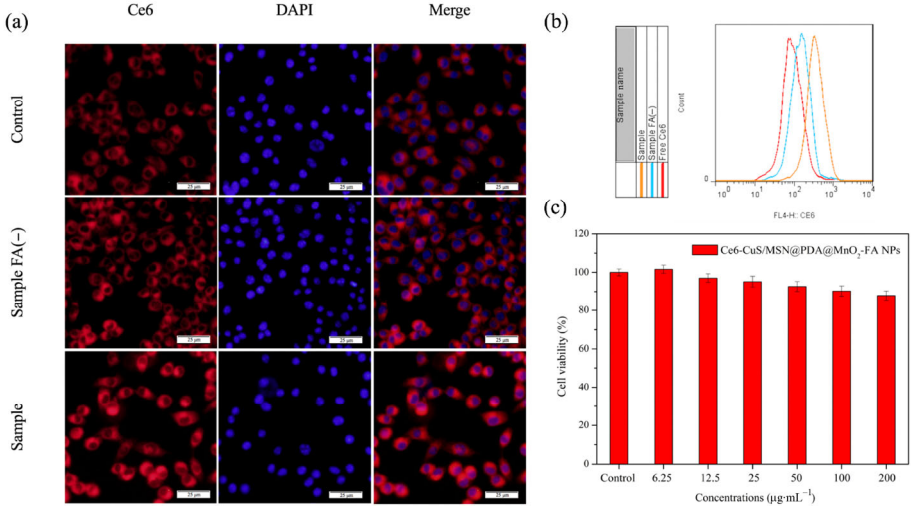

Figure 4 (a) Fluorescence images of 4T1 cells incubated with free Ce6, sample FA(−) and sample for 2 h. Scale bar = 25 μm. (b) The flow cytometric histogram profiles of 4T1 cells incubated with free Ce6, sample FA(−) and sample for 2 h. Sample FA(−) = Ce6-CuS/MSN@PDA@MnO_2 NPs, sample = Ce6-CuS/MSN@PDA@MnO_2-FA NPs. (c) Cell viability of 4T1 cells incubated with Ce6-CuS/MSN@PDA@MnO_2-FA NPs for 24 h.

of the NPs through fluorescence intensity comparison (Fig. 4(a)) and flow cytometry analysis (Fig. 4(b)). The cytotoxicity of the Ce6-CuS/MSN@PDA@MnO_2-FA NPs against 4T1 cells was studied using a standard MTT assay. As shown in Fig. 4(c), the cell viability at different Ce6-CuS/MSN@PDA@MnO_2-FA NPs concentrations (0–200 μg·mL^{-1}) remained over 85% after 24 h incubation. These low dark cytotoxicity and high cellular uptake efficiency make Ce6-CuS/MSN@PDA@MnO_2-FA NPs ideal for our proposed therapeutic application.

3.3 ROS generation

The ability for Ce6-CuS/MSN@PDA@MnO_2-FA NPs to generate $^1O_2$ was evaluated by electron paramagnetic resonance (EPR) spectroscopy with spin-trapping agent TMPD [36]. As shown in Fig. 5(a), 660 nm laser irradiation on the dispersion of Ce6-CuS/MSN@PDA@MnO_2-FA NPs produced a typical EPR spectrum of 2,2,6,6-tetramethyl-4-piperidone-1-oxyl, revealing the generation of $^1O_2$. Moreover, these EPR signals were intensified with the presence of H_2O_2, suggesting that our NPs can make use of H_2O_2 to produce $^1O_2$ as designed. The results obtained from fluorescent DCFH-DA assay also gave consistent results (Fig. 5(b)).

The DCFH-DA probe was also used to investigate the intracellular ROS production by our NPs, with the working principle that the non-fluorescent DCFH-DA converts to non-fluorescent DCFH after entering cells and reacting with ROS to give fluorescent 2',7'-dichlorofluorescein (DCF) [36]. As depicted in Fig. 5(c), typical DCF fluorescent signal was detected in 4T1 cells incubated with Ce6-CuS/MSN@PDA@MnO_2-FA NPs and DCFH-DA and irradiated with 660 nm laser. Weaker fluorescent signal was detected when the non-MnO_2-functionalized congener Ce6-CuS/MSN@PDA-FA NPs were used, revealing the important role of MnO_2 nano-sheets.

3.4 *In vitro* photocytotoxicity

The photocytotoxicity of Ce6-CuS/MSN@PDA@MnO_2-FA NPs was first investigated by a standard MTT assay with 660 nm laser (50 mW·cm^{-2}) or 808 nm laser (2 W·cm^{-2}) irradiation alone for 10 min. As shown in Fig. 6(a), using 660 or 808 nm laser alone only led to insignificant damage to 4T1 cells (cell

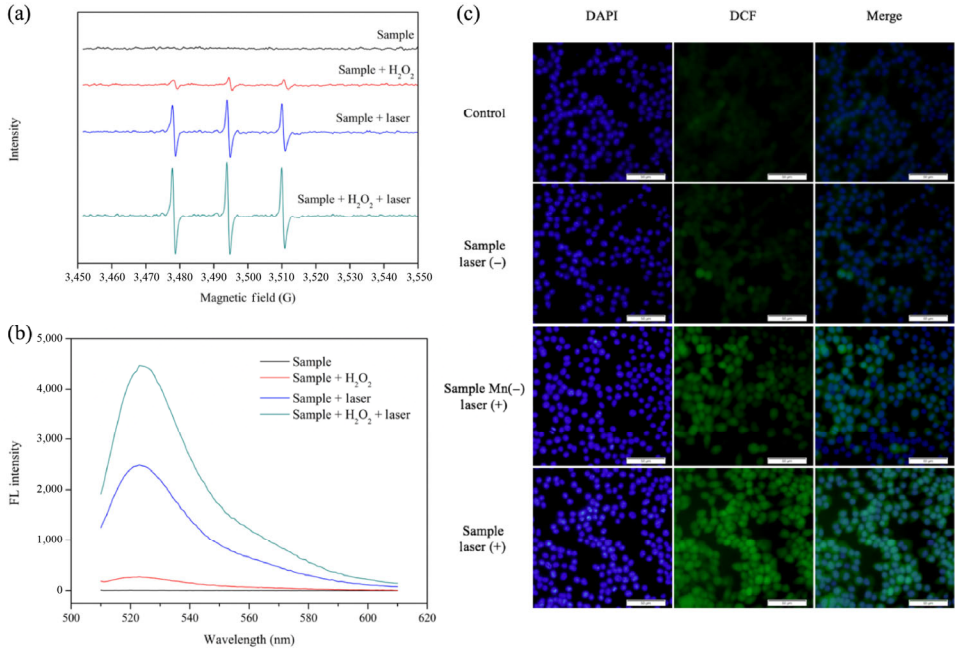

Figure 5 (a) 2,2,6,6-Tetramethyl-4-piperidone-1-oxyl (TEMPONE) EPR signal produced by the sample and spin-trapping agent TMPD under 660 nm laser irradiation (50 mW·cm^{-2}) in the presence of H_2O_2. (b) Fluorescence spectra of ROS generation by the sample/H_2O_2 mixture under 660 nm laser irradiation (50 mW·cm^{-2}). (c) Confocal laser scanning microscopy images of ROS generation by the sample in 4T1 cells. Sample = Ce6-CuS/MSN@PDA@MnO_2-FA NPs, sample Mn(–) = Ce6-CuS/MSN@PDA-FA NPs, laser (+) = with 660 nm laser treatment, laser (–) = without 660 nm laser treatment. Scale bars = 50 μm.

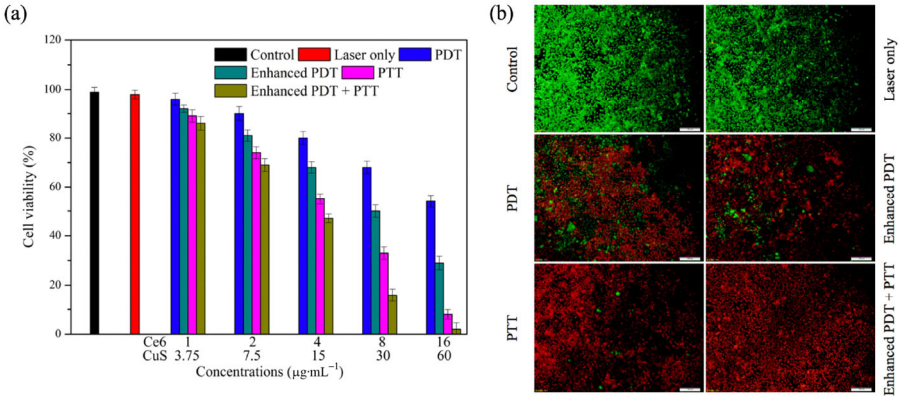

Figure 6 (a) The 24 h cell viability of 4T1 cells treated with 660 nm/808 nm laser (laser only), Ce6-CuS/MSN@PDA-FA NPs + 660 nm laser (PDT), Ce6-CuS/MSN@PDA@MnO_2-FA NPs + 660 nm laser (enhanced PDT), Ce6-CuS/MSN@PDA@MnO_2-FA NPs + 808 nm laser (PTT), Ce6-CuS/MSN@PDA@MnO_2-FA NPs + 660 nm/808 nm laser (enhanced PDT + PTT) and a blank group as control. (b) Fluorescence images of 4T1 cells co-stained with PI and Calcein-AM after treatment. Scale bar = 100 μm.

viability > 95%). A dose-dependent PDT effect was observed for the non-MnO_2-functionalized Ce6-CuS/MSN@PDA-FA NPs under 660 nm laser irradiation (50 mW·cm^{-2}), and a cell viability of 54% was recorded when the concentration of Ce6 was 16 μg·mL^{-1}. Significantly, the cell viability decreased to 29% if Ce6-CuS/MSN@PDA@MnO_2-FA NPs with the same Ce6 concentration was employed, signifying the importance of incorporating MnO_2 nano-sheets in our design. Dose-dependent PTT effect was also observed for Ce6-CuS/MSN@PDA@MnO_2-FA NPs under 808 nm laser irradiation (2 W·cm^{-2}). Encouragingly, a cell viability of 2% could be achieved when a combination of 660 and 808 nm laser irradiation was used with Ce6-CuS/MSN@PDA@MnO_2-FA NPs (concentrations of Ce6 and CuS were 16 and 60 μg·mL^{-1}, respectively). These results clearly demonstrated the remarkable synergistic PDT/PTT effects for Ce6-CuS/MSN@PDA@MnO_2-FA NPs.

To visualize the combined photo-killing effects of Ce6-CuS/MSN@PDA@MnO_2-FA NPs, the 4T1 cells were co-stained with Calcein-AM and PI for live and dead cell imaging respectively after different treatments. As shown in Fig. 6(b), the control and laser-only groups showed a vivid green fluorescence from Calcein-AM, indicating negligible cell damage. On the other hand, groups with laser and Ce6-CuS/MSN@PDA-FA or Ce6-CuS/MSN@PDA@MnO_2-FA NPs treatments resulted in different degrees of cell death as suggested by the presence of red fluorescence from PI. Consistent with the photocytotoxicity study aforementioned, the most remarkable therapeutic result came from the combination of 660 and 808 nm laser irradiation with Ce6-CuS/MSN@PDA@MnO_2-FA NPs, where no surviving cells could be observed.

3.5 *In vitro* and *in vivo* imaging

Since Mn^{2+} has the ability to shorten the longitudinal T_1 of protons in water [36, 37], the MR imaging potential of Ce6-CuS/MSN@PDA@MnO_2-FA NPs was evaluated. As shown in Fig. 7(a), the NPs dispersions showed typical *in vitro* T_1-weighted MR images, and the brightness increased gradually with concentration. The brightness of the MR images could be increased when the NPs were dispersed in acidified H_2O_2 solution, an expected result from the increased production of Mn^{2+} in accordance with the equations depicted in Scheme 1. The r_1 was calculated to be 10.41 mM^{-1}·s^{-1} in H_2O_2 solution at pH 5.0 (Fig. 7(b)), which is 2 times higher than that of the clinical MR imaging agent Magnevist® [38]. For *in vivo* MR imaging, a NPs dispersion (10 mg·kg^{-1}) was intravenously injected into 4T1 tumor-bearing balb/c mice and the MR images were collected at different points in time. The T_1-weighted MR imaging signals of the tumor region strengthened and reached the maximum at 12 h post-injection (Fig. 7(c)), suggesting an effective accumulation of the Ce6-CuS/MSN@PDA@MnO_2-FA NPs within tumor cells. Additionally, the MR contrast at the tumor site showed a decrease over time, as the related MR imaging signal changes recorded in Fig. 7(d). This decease may be due to the partial clearance of the NPs. All these results signified that our system can act as potent MR imaging contrast agent for cancer diagnosis.

3.6 *In vivo* therapeutic efficacy and histological analysis

The photo-induced temperature changes of the Ce6-CuS/MSN@PDA@MnO_2-FA NPs on the 4T1 tumor-bearing balb/c mice were recorded by an infrared thermal camera (Fig. 8(a)). The accumulated NPs in the tumor site could efficiently convert the NIR light into local heat, showing a significant temperature increase from 31.5 to 51.8 °C when exposed to 808 nm laser irradiation for 10 min (2 W·cm^{-2}) at 12 h post-injection, whereas the PBS-injected group exhibited only a minimal temperature elevation from 30.0 to 32.5 °C. These results revealed the excellent *in vivo* photothermal performance of the Ce6-CuS/MSN@PDA@MnO_2-FA NPs to be used for tumor ablation.

To further investigate the *in vivo* synergistic PDT/PTT effects, 4T1 tumor-bearing mice were treated in 5 groups (n = 5 per group): (1) PBS (control), (2) Ce6-CuS/MSN@PDA-FA

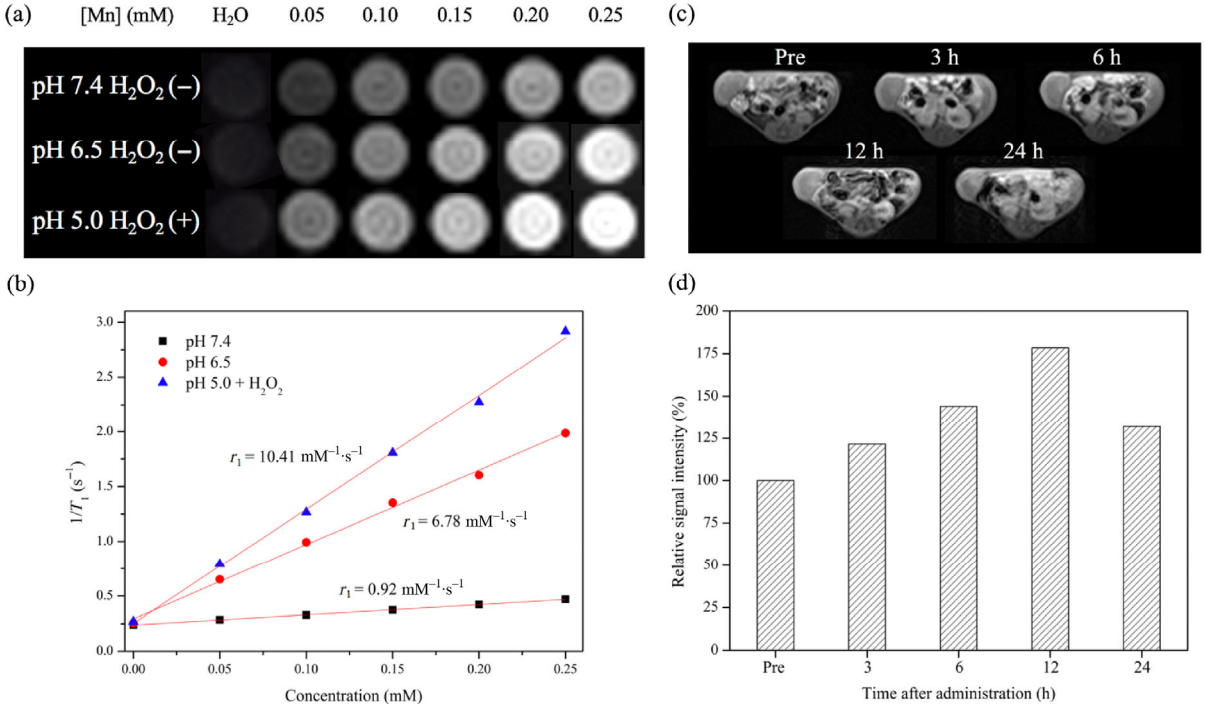

Figure 7 (a) T_1-weighted MR images of pure water, Ce6-CuS/MSN@PDA@MnO_2-FA NPs with different Mn concentrations under pH 7.4 and 6.5 without H_2O_2, and pH 5.0 with H_2O_2. [H_2O_2] = 100 μM. (b) The corresponding relaxation rate ($1/T_1$) as a function of Mn concentration (mM) of Ce6-CuS/MSN@PDA@MnO_2-FA NPs dispersion. (c) T_1-weighted MR images and (d) relative signal intensity of 4T1 tumor acquired at different time points after injection of Ce6-CuS/MSN@PDA@MnO_2-FA NPs dispersion. Pre = before injection.

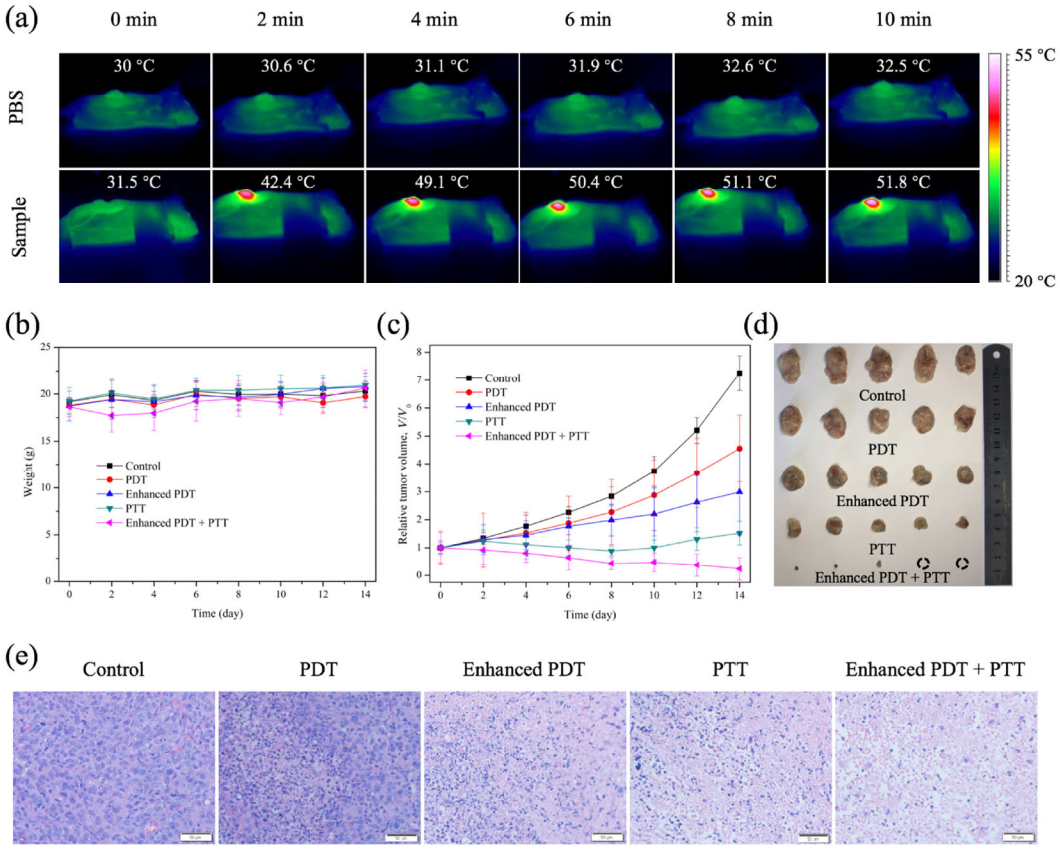

Figure 8 (a) Thermal imaging of 4T1 tumor after injection of PBS or Ce6-CuS/MSN@PDA@MnO_2-FA NPs followed by exposure to an 808 nm NIR laser (2 W·cm^{-2}) for 10 min. (b) Body weight changes and (c) the relative tumor growth curves of post-treatment mice in all groups. PBS (control), Ce6-CuS/MSN@PDA-FA NPs + 660 nm laser (PDT), Ce6-CuS/MSN@PDA@MnO_2-FA NPs + 660 nm laser (enhanced PDT), Ce6-CuS/MSN@PDA@MnO_2-FA NPs + 808 nm laser (PTT), Ce6-CuS/MSN@PDA@MnO_2-FA NPs + 660 nm/808 nm laser (enhanced PDT + PTT). (d) Photos of the corresponding changes in tumor volume after treatment in all groups. (e) H&E staining images of the tumor slices after different treatment. Scale bars = 50 μm.

NPs + 660 nm laser (PDT), (3) Ce6-CuS/MSN@PDA@MnO_2-FA NPs + 660 nm laser (enhanced PDT), (4) Ce6-CuS/MSN@PDA@MnO_2- FA NPs + 808 nm laser (PTT), and (5) Ce6-CuS/MSN@PDA@MnO_2-FA NPs + 660 nm/808 nm laser (enhanced PDT + PTT). The body weight and tumor size of the treated mice in each group were measured for 14 days. No obvious decrease of body weight was found in all the groups, implying the low cytotoxicity of the synthesized NPs during the therapy process (Fig. 8(b)). As displayed in Fig. 8(c), the tumor size of control group increased rapidly, consistent with the fact that PBS solution could not inhibit tumor growth. In contrast, the tumor size of PDT, enhanced PDT and PTT groups showed some degree of restraint due to the single PDT or PTT effect. The enhanced PDT group displayed a higher tumor size suppression than the PDT group, demonstrating the role of MnO_2 nano-sheet in enhancing PDT. In addition, it is noteworthy that the enhanced PDT + PTT group exhibited much higher therapeutic efficiency over any other single modality treatment group. The tumors in this group were almost completely destroyed after 2 weeks of treatment (Fig. 8(d)), revealing the synergistically enhanced PDT/PTT effect of Ce6-CuS/MSN@PDA@MnO_2-FA NPs. Sections from the tumors and major organs were then collected from the mice for histological analysis by hematoxylin-eosin (H&E) staining. As shown in Fig. 8(e), no necrosis or obvious apoptosis was observed in the tumor tissue of the control group, whereas a certain degree of tissue and cellular destruction were observed from PDT, enhanced PDT and PTT groups. More importantly, substantial nuclear shrinkage and cytoplasm leakage in apoptotic cells were observed from the enhanced PDT + PTT group. These results further demonstrated the feasibility of Ce6-CuS/MSN@PDA@MnO_2-FA NPs serving as a highly effective PDT/PTT dual-modal therapeutic agent. In addition, all H&E staining images of the major organs showed insignificant tissue damage (Fig. S7 in the ESM), suggesting the biological safety of Ce6-CuS/MSN@PDA@MnO_2-FA NPs for potential clinical application. Blood circulation and biodistribution of the Ce6-CuS/MSN@PDA@MnO_2-FA NPs were also studied by measuring the copper levels. The results showed that copper concentration in the blood decreased gradually while large number of Ce6-CuS/MSN@PDA@MnO_2-FA NPs accumulated in the tumor site (Fig. S8 in the ESM).

4 Conclusions

In summary, a multifunctional nano-theranostic system was proposed for tumor-specific MR imaging and synergistic PDT/PTT. The Ce6-CuS/MSN@PDA@MnO_2-FA NPs possessed low cytotoxicity and enhanced cellular uptake, allowing efficient accumulation in the tumor site for precise cancer diagnosis. The outer MnO_2 nano-sheets provided sufficient O_2 using endogenous H_2O_2 as feedstock to relieve tumor hypoxia for PDT. Remarkable photothermal performance was also displayed due to the coexistence of the inner CuS NPs and PDA coating. The therapeutic outcomes are exceptional as the NPs efficiently suppressed the tumor growth owing to the enhanced PDT and PTT synergistic treatment. In addition, our work not only constructed a potential tumor-targeting theranostic agent but also paved a way to develop a rich variety of novel structures for various biomedical applications.

Acknowledgements

The work described in this paper was supported by the Research Grants Council of Hong Kong SAR (CityU 11228316, 11207117, and T42-103/16-N), City University of Hong Kong (Nos. 7005096 and 7005257) and the National Natural Science Foundation of China (No. 81874084).

Electronic Supplementary Material: Supplementary material (further details of characterization of the samples, *in vitro* O_2 generation, singlet oxygen detection, photothermal performance measurement, cellular uptake and cytotoxicity, photocytotoxicity, animal and tumor models, *in vitro* and *in vivo* imaging, *in vivo* synergistic PDT/PTT and histopathological analysis, blood circulation and biodistribution, and supplementary figures including the high resolution TEM images, XRD patterns, physiological stability test, UV–vis–NIR absorption spectra, H&E staining images of the major organs, and blood circulation and biodistribution studies) is available in the online version of this article at https://doi.org/10.1007/s12274-020-2646-7.

References

[1] Yang, T.; Tang, Y. A.; Liu, L.; Lv, X. Y.; Wang, Q. L.; Ke, H. T.; Deng, Y. B.; Yang, H.; Yang, X. L.; Liu, G. et al. Size-dependent Ag_2S nanodots for second near-infrared fluorescence/photoacoustics imaging and simultaneous photothermal therapy. *ACS Nano* **2017**, *11*, 1848–1857.

[2] Deng, Y. Y.; Jia, F.; Chen, S. Y.; Shen, Z. D.; Jin, Q.; Fu, G. S.; Ji, J. Nitric oxide as an all-rounder for enhanced photodynamic therapy: Hypoxia relief, glutathione depletion and reactive nitrogen species generation. *Biomaterials* **2018**, *187*, 55–65.

[3] Wang, B.; Lin, W. M.; Mao, Z. W.; Gao, C. Y. Near-infrared light triggered photothermal therapy and enhanced photodynamic therapy with a tumor-targeting hydrogen peroxide shuttle. *J. Mater. Chem. B* **2018**, *6*, 3145–3155.

[4] Yang, Y.; Zhu, W. J.; Feng, L. Z.; Chao, Y.; Yi, X.; Dong, Z. L.; Yang, K.; Tan, W. H.; Liu, Z.; Chen, M. W. G-quadruplex-based nanoscale coordination polymers to modulate tumor hypoxia and achieve nuclear- targeted drug delivery for enhanced photodynamic therapy. *Nano Lett.* **2018**, *18*, 6867–6875.

[5] Chen, Q.; Wang, C.; Cheng, L.; He, W. W.; Cheng, Z. P.; Liu, Z. Protein modified upconversion nanoparticles for imaging-guided combined photothermal and photodynamic therapy. *Biomaterials* **2014**, *35*, 2915–2923.

[6] Zhang, D.; Wu, M.; Zeng, Y. Y.; Wu, L. J.; Wang, Q. T.; Han, X.; Liu, X. L.; Liu, J. F. Chlorin e6 conjugated poly (dopamine) nanospheres as PDT/PTT dual-modal therapeutic agents for enhanced cancer therapy. *ACS Appl. Mater. Interfaces* **2015**, *7*, 8176–8187.

[7] Zhu, H. J.; Li, J. C.; Qi, X. Y.; Chen, P.; Pu, K. Y. Oxygenic hybrid semiconducting nanoparticles for enhanced photodynamic therapy. *Nano Lett.* **2018**, *18*, 586–594.

[8] Ren, H.; Liu, J. Q.; Su, F. H.; Ge, S. Z.; Yuan, A. H.; Dai, W. M.; Wu, J. H.; Hu, Y. Q. Relighting photosensitizers by synergistic integration of albumin and perfluorocarbon for enhanced photodynamic therapy. *ACS Appl. Mater. Interfaces* **2017**, *9*, 3463–3473.

[9] Liu, J. T.; Du, P.; Mao, H.; Zhang, L.; Ju, H. X.; Lei, J. P. Dual-triggered oxygen self-supply black phosphorus nanosystem for enhanced photodynamic therapy. *Biomaterials* **2018**, *172*, 83–91.

[10] Gao, M.; Liang, C.; Song, X. J.; Chen, Q.; Jin, Q. T.; Wang, C.; Liu, Z. Erythrocyte-membrane-enveloped perfluorocarbon as nanoscale artificial red blood cells to relieve tumor hypoxia and enhance cancer radiotherapy. *Adv. Mater.* **2017**, *29*, 1701429.

[11] Song, X. J.; Feng, L. Z.; Liang, C.; Yang, K.; Liu, Z. Ultrasound triggered tumor oxygenation with oxygen-shuttle nanoperfluorocarbon to overcome hypoxia-associated resistance in cancer therapies. *Nano Lett.* **2016**, *16*, 6145–6153.

[12] Li, R. Q.; Zhang, C.; Xie, B. R.; Yu, W. Y.; Qiu, W. X.; Cheng, H.; Zhang, X. Z. A two-photon excited O_2-evolving nanocomposite for efficient photodynamic therapy against hypoxic tumor. *Biomaterials* **2019**, *194*, 84–93.

[13] Wang, H. R.; Chao, Y.; Liu, J. J.; Zhu, W. W.; Wang, G. L.; Xu, L. G.; Liu, Z. Photosensitizer-crosslinked *in-situ* polymerization on catalase for tumor hypoxia modulation & enhanced photodynamic therapy. *Biomaterials* **2018**, *181*, 310–317.

[14] Kim, J.; Cho, H. R.; Jeon, H.; Kim, D.; Song, C.; Lee, N.; Choi, S. H.; Hyeon, T. Continuous O_2-evolving $MnFe_2O_4$ nanoparticle-anchored mesoporous silica nanoparticles for efficient photodynamic therapy in hypoxic cancer. *J. Am. Chem. Soc.* **2017**, *139*, 10992–10995.

[15] Liu, Y.; Zhen, W. Y.; Wang, Y. H.; Liu, J. H.; Jin, L. H.; Zhang, T. Q.; Zhang, S. T.; Zhao, Y.; Song, S. Y.; Li, C. Y. et al. One-dimensional Fe_2P acts as a fenton agent in response to NIR II light and ultrasound for deep tumor synergetic theranostics. *Angew. Chem., Int. Ed.* **2019**, *58*, 2407–2412.

[16] Yang, Z. L.; Tian, W.; Wang, Q.; Zhao, Y.; Zhang, Y. L.; Tian, Y.; Tang, Y. X.; Wang, S. J.; Liu, Y.; Ni, Q. Q. et al. Oxygen-evolving mesoporous organosilica coated prussian blue nanoplatform for highly efficient photodynamic therapy of tumors. *Adv. Sci.* **2018**, *5*, 1700847.

[17] Wei, J. P.; Li, J. C.; Sun, D.; Li, Q.; Ma, J. Y.; Chen, X. L.; Zhu, X.; Zheng, N. F. A novel theranostic nanoplatform based on Pd@Pt-PEG-Ce6 for enhanced photodynamic therapy by modulating tumor hypoxia microenvironment. *Adv. Funct. Mater.* **2018**, *28*, 1706310.

[18] Xu, J. T.; Han, W.; Yang, P. P.; Jia, T.; Dong, S. M.; Bi, H. T.; Gulzar, A.; Yang, D.; Gai, S. L.; He, F. et al. Tumor microenvironment-responsive mesoporous MnO_2-coated upconversion nanoplatform for self-enhanced tumor theranostics. *Adv. Funct. Mater.* **2018**, *28*, 1803804.

[19] Zhang, W. T.; Li, S. H.; Liu, X. N.; Yang, C. Y.; Hu, N.; Dou, L. N.; Zhao, B. X.; Zhang, Q. Y.; Suo, Y. R.; Wang, J. L. Oxygen-generating MnO_2 nanodots-anchored versatile nanoplatform for combined chemo-photodynamic therapy in hypoxic cancer. *Adv. Funct. Mater.* **2018**, *28*, 1706375.

[20] Gao, S.; Wang, G. H.; Qin, Z. N.; Wang, X. Y.; Zhao, G. Q.; Ma, Q. J.; Zhu, L. Oxygen-generating hybrid nanoparticles to enhance fluorescent/photoacoustic/ultrasound imaging guided tumor photodynamic therapy. *Biomaterials* **2017**, *112*, 324–335.

[21] Lin, T. S; Zhao, X. Z.; Zhao, S.; Yu, H.; Cao, W. M.; Chen, W.; Wei, H.; Guo, H. Q. O_2-generating MnO_2 nanoparticles for enhanced photodynamic therapy of bladder cancer by ameliorating hypoxia. *Theranostics* **2018**, *8*, 990–1004.

[22] Fan, H. H; Yan, G. B.; Zhao, Z. L.; Hu, X. X.; Zhang, W. H.; Liu, H.; Fu, X. Y.; Fu, T.; Zhang, X. B.; Tan, W. H. A smart photosensitizer–manganese dioxide nanosystem for enhanced photodynamic therapy by reducing glutathione levels in cancer cells. *Angew. Chem., Int. Ed.* **2016**, *55*, 5477–5482.

[23] Liu, B.; Li, C. X.; Chen, G. Y.; Liu, B.; Deng, X. R.; Wei, Y.; Xia, J.; Xing, B. G.; Ma, P. A.; Lin, J. Synthesis and optimization of MoS_2@Fe_3O_4-ICG/Pt(IV) nanoflowers for MR/IR/PA bioimaging and combined PTT/PDT/chemotherapy triggered by 808 nm laser. *Adv. Sci.* **2017**, *4*, 1600540.

[24] Li, P. S.; Liu, L.; Lu, Q. L.; Yang, S.; Yang, L. F.; Cheng, Y.; Wang, Y. D.; Wang, S. Y.; Song, Y. L.; Tan, F. P. et al. Ultrasmall MoS_2 nanodots-doped biodegradable SiO_2 nanoparticles for clearable FL/CT/MSOT imaging-guided PTT/PDT combination tumor therapy. *ACS Appl. Mater. Interfaces* **2019**, *11*, 5771–5781.

[25] Yang, C. Y.; Yu, H. H.; Gao, Y.; Guo, W.; Li, Z. Z.; Chen, Y. D.; Pan, Q. M.; Ren, M. X.; Han, X. J.; Guo, C. S. Surface-engineered vanadium nitride nanosheets for an imaging-guided photothermal/photodynamic platform of cancer treatment. *Nanoscale* **2019**, *11*, 1968–1977.

[26] You, Q.; Sun, Q.; Wang, J. P.; Tan, X. X.; Pang, X. J.; Liu, L.; Yu, M.; Tan, F. P.; Li, N. A single-light triggered and dual-imaging guided multifunctional platform for combined photothermal and photodynamic therapy based on TD-controlled and ICG-loaded CuS@mSiO_2. *Nanoscale* **2017**, *9*, 3784–3796.

[27] Goel, S.; Ferreira, C. A.; Chen, F.; Ellison, P. A.; Siamof, C. M.; Barnhart, T. E.; Cai, W. B. Activatable hybrid nanotheranostics for tetramodal imaging and synergistic photothermal/photodynamic therapy. *Adv. Mater.* **2018**, *30*, 1704367.

[28] Chang, D. F.; Gao, Y. F.; Wang, L. J.; Liu, G.; Chen, Y. H.; Wang, T.;

Tao, W.; Mei, L.; Huang, L. Q.; Zeng, X. W. Polydopamine-based surface modification of mesoporous silica nanoparticles as pH-sensitive drug delivery vehicles for cancer therapy. *J. Colloid Interface Sci.* **2016**, *463*, 279–287.

[29] Li, Y. Z.; Zhao, R.; Chao, S.; Sun, B. L.; Wang, C.; Li, X. Polydopamine coating assisted synthesis of MnO_2 loaded inorganic/organic composite electrospun fiber adsorbent for efficient removal of Pb^{2+} from water. *Chem. Eng. J.* **2018**, *344*, 277–289.

[30] Cheng, W.; Nie, J. P.; Xu, L.; Liang, C. Y.; Peng, Y. M.; Liu, G.; Wang, T.; Mei, L.; Huang, L. Q.; Zeng, X. W. pH-sensitive delivery vehicle based on folic acid-conjugated polydopamine-modified mesoporous silica nanoparticles for targeted cancer therapy. *ACS Appl. Mater. Interfaces* **2017**, *9*, 18462–18473.

[31] Xiao, D.; Jia, H. Z.; Zhang, J.; Liu, C. W.; Zhuo, R. X.; Zhang, X. Z. A dual-responsive mesoporous silica nanoparticle for tumor-triggered targeting drug delivery. *Small* **2014**, *10*, 591–598.

[32] Zhang, L.; Yang, Z.; Zhu, W.; Ye, Z. L.; Yu, Y. M.; Xu, Z. S.; Ren, J. H.; Li, P. H. Dual-stimuli-responsive, polymer-microsphere-encapsulated CuS nanoparticles for magnetic resonance imaging guided synergistic chemo-photothermal therapy. *ACS Biomater. Sci. Eng.* **2017**, *3*, 1690–1701.

[33] Liu, X. M.; Yang, T. S.; Han, Y. F.; Zou, L.; Yang, H. R.; Jiang, J. Y.; Liu, S. J.; Zhao, Q.; Huang, W. *In situ* growth of CuS/SiO_2-based multifunctional nanotherapeutic agents for combined photodynamic/photothermal cancer therapy. *ACS Appl. Mater. Interfaces* **2018**, *10*, 31008–31018.

[34] Zhang, W. H.; Shi, J. L.; Chen, H. R.; Hua, Z. L.; Yan, D. S. Synthesis and characterization of nanosized ZnS confined in ordered mesoporous silica. *Chem. Mater.* **2001**, *13*, 648–654.

[35] Wang, Z. Z.; Zhang, Y.; Ju, E. G.; Liu, Z.; Cao, F. F.; Chen, Z. W.; Ren, J. S.; Qu, X. G. Biomimetic nanoflowers by self-assembly of nanozymes to induce intracellular oxidative damage against hypoxic tumors. *Nat. Commun.* **2018**, *9*, 3334.

[36] Zhu, W.; Zhang, L.; Yang, Z.; Liu, P.; Wang, J.; Cao, J. G.; Shen, A. G.; Xu, Z. S.; Wang, J. An efficient tumor-inducible nanotheranostics for magnetic resonance imaging and enhanced photodynamic therapy. *Chem. Eng. J.* **2019**, *358*, 969–979.

[37] He, Z. M.; Xiao, Y.; Zhang, J. R.; Zhang, P. H.; Zhu, J. J. *In situ* formation of large pore silica–MnO_2 nanocomposites with H^+/H_2O_2 sensitivity for O_2-elevated photodynamic therapy and potential MR imaging. *Chem. Commun.* **2018**, *54*, 2962–2965.

[38] Liu, R. Q.; Liang, S.; Jiang, C.; Zhang, L.; Yuan, T. M.; Li, P. H.; Xu, Z. S.; Xu, H. B.; Chu, P. K. Smart polymeric particle encapsulated gadolinium oxide and europium: Theranostic probes for magnetic resonance/ optical imaging and antitumor drug delivery. *J. Mater. Chem. B* **2016**, *4*, 1100–1107.